Environmental Science and Pollution Research
https://doi.org/10.1007/s11356-019-05498-z

RESEARCH ARTICLE

Influence of preparation method on structural, optical, magnetic, and adsorption properties of nano-$NiFe_2O_4$

Samah Samy Selima[1] · Mohamed Khairy[1,2] · Wafaa Abdallah Bayoumy[1] · Mahmoud Ahmed Mousa[1]

Received: 16 March 2019 / Accepted: 15 May 2019

Abstract

Nickel ferrite ($NiFe_2O_4$) nanoparticles are prepared through different routes (microwave, co-precipitation, and pyrolysis) and tested for water purification applications through adsorption removal of an acid red dye B as a model organic pollutant. The characterizations of the prepared samples were done using XRD, FT-IR, SEM, TEM, BET, UV-Vis absorbance, Raman spectrum, and vibrating sample magnetometer (VSM). All samples showed an inverse spinel crystal structure. The obtained results pointed out to the effect of the synthetic route on the morphology, particle size, optical, and magnetic properties of the prepared ferrites. Magnetic measurements showed super-paramagnetic behavior for all samples. The magnetic saturation (M_s) of the sample prepared by pyrolysis, was found to possess the highest saturation value, 34.8 emu/g. Adsorption experiments were performed under the change in several parameters, such as pH, adsorbent dosage, and initial dye concentration. A dye removal percentage of 99% was reached under the optimum state. The isothermal adsorption of the acid red dye was investigated using several models, in which the experimental data could be best described by the Freundlich model. Several kinetic and equilibrium models were inspected by linear regression analysis and showed best fitting for the adsorption data through pseudo-second-order model. The calculated thermodynamic parameters indicated that the adsorption of acid red dye onto all the ferrite samples is a spontaneous and endothermic physical adsorption process.

Keywords $NiFe_2O_4$ · Magnetic properties · Ferrite · Thermodynamic parameters

Introduction

The wastewater from different industries is a major hazard for the aquatic environment. Organic dyes are one of the largest groups of contaminants discharged into wastewater from textile, dyeing, and other industrial activities. Hence, these dyes must be removed or degraded before being discharged into the environment. Dyes are classified into anionic, cationic, and non-ionic dyes. The deletion of anionic dyes is considered the most challenging task as they are water soluble and generate very bright colors in water with acidic properties (Gómez et al. 2007).

Many physical, chemical, and biological methods, such as adsorption, zonation, precipitation, flocculation, reverse osmosis, ultra-filtration, and biodegradation, have been used for dye removal from wastewaters (Dawood and Sen 2014; Mahmoodi et al. 2014). Conventional methods are costly and produce numerous side effects. However, the adsorption technique is relatively widespread due to its simplicity and high efficiency, in addition to the convenience of an extensive scope of adsorbents (Allen 1996). Generally, adsorbent handled is smaller in size, because the smaller size adsorbents have higher surface area conducting to greatest adsorption capacity. But, it is hard to withdraw them from the water after attaining saturated adsorption.

Recently, magnetic nanoparticles consider as a promising approach for the adsorption process in separation methods (Farghali et al. 2013; Ismail et al. 2013; Wang et al. 2012). By applying a low-intensity magnetic field, the magnetic

Responsible editor: Tito Roberto Cadaval Jr

Electronic supplementary material The online version of this article (https://doi.org/10.1007/s11356-019-05498-z) contains supplementary material, which is available to authorized users.

✉ Samah Samy Selima
samah_selima@yahoo.com

[1] Chemistry Department, Faculty of Science, Benha University, Benha, Egypt

[2] Chemistry Department, College of Science, Imam Mohammad Ibn Saud Islamic University, Riyadh, Kingdom of Saudi Arabia

Published online: 24 May 2019

nanoparticles are going to be separated by the applied magnetic force. Nickel ferrite is one of the most useful magnetic materials owing to its high-saturation magnetization and high chemical and electrochemical stability that sort it as an effective and qualified adsorbent (Goldman 2006; Gunjakar et al. 2008).

The nickel ferrite is an inverse spinel, in which eight molecules of $NiFe_2O_4$ presents into one lattice of the spinel structure. The physical properties of spinel ferrites depend on the type of cations, their charges, and their spreading in each of tetrahedral (A) and octahedral (B) lattice sites. In the inverse, spinel half of Fe^{3+} ions favorably occupy the tetrahedral positions (8A-sites), whereas the other files, the octahedral sites (16B-sites). So, it is generally symbolized by the formula $(Fe^{3+})[Ni^{2+}Fe^{3+}]O_4^{-2}$, where the round and the square denote tetrahedral and octahedral positions, respectively (Carta et al. 2009).

Synthesis procedure is a central tool for the production of nanocrystalline materials with request morphological structure and properties. Therefore, the present work was designed to study the effect of the synthetic method on structural, particle size, surface area, morphology, optical, and magnetic properties of $NiFe_2O_4$ nanoparticles. Moreover, we assessed the effectiveness of the synthesized magnetic ferrite samples for removing acid red B (ARB) from aqueous solution, as a model pollutant, by adsorption technique. The dye adsorption process has been investigated via kinetics, equilibrium, and thermodynamic approaches.

Experimental

Materials

All chemicals were analytical and reagent grade and used without further purification. Double distilled water was used throughout all the experiments.

Synthesis of samples

$NiFe_2O_4$ samples were prepared by various methods: a microwave hydrothermal, a polymer-pyrolysis, and co-precipitation.

Microwave method

We mixed $Ni(NO_3)_2{\cdot}6H_2O$) and $Fe(NO_3)_3{\cdot}9H_2O$ with molar ratio of Ni/Fe = 1:2 in 6 M of aqueous KOH. The mixture was then transferred into a Teflon reactor and loaded into a microwave oven (MARS 5, CEM Comp) and heated up to 573 K for 40 min and then cooled to room temperature. The powder obtained was filtered, washed with distilled water five times, and dried at 373 K for 1 h (Sonali et al. 2009). The sample was denoted as NiF_{micr}.

Polymer-pyrolysis method

In this method, nickel ferrite was synthesized by a pyrolysis method using metal polyacrylate of Ni^{2+} and Fe^{3+}. The precursor was made by polymerization of acrylic acid in the existence of metal salts Ni $(NO_3)_2{\cdot}6H_2O$ and $Fe(NO_3)_3{\cdot}9H_2O$, with molar fraction of Ni/Fe = 1:2, as well as small amount of $(NH_4)_2S_2O_8$ as an initiator. The metal polyacrylate obtained was dried at 383 K for 18 h, calcined at 768 K for 4 h in air, and finally cooled slowly to room temperature (Liu et al. 2007). The sample is defined as NiF_{poly}.

Co-precipitation method

We dissolved nickel and iron nitrate with 1:2 molar ratio in distilled water under constant stirring at 358 K. The solution was precipitated by urea, filtered, and washed four times with distilled water and dried in an oven at 405 K for 16 h. Finally, the powder obtained was crushed and calcined at 768 K for 5 h (Reddy et al. 1999). The sample is denoted as NiF_{ppt}.

Characterization methods

The XRD patterns of the ferrite samples were recorded for 2θ from 10° to 80° at a scan rate of 2° min^{-1} using X-ray diffraction (Philips PW-3710 diffractometer), Cu Ka (l = 0.15406 nm) radiation. The FTIR analysis was carried out by a Thermo Scientific spectrometer using a KBr pelletizer with a scanning region of 4000–400 cm^{-1}. The morphological properties were examined by a scanning electron microscope (SEM) (JEOL-JSM 6360 unit) and transmission electron microscope (TEM) (Philips CM-12 unit). The surface properties were determined by BET technique using the adsorption of nitrogen gas at liquid nitrogen temperature (Lowell et al. 2004). UV-Vis diffuse reflectance spectra recorded on a UV4 Unicam spectrophotometer in the range 200–800 nm. Magnetic measurements were carried out at room temperature using a vibrating sample magnetometer (VSM) (model 7407 Lakeshore) with a maximum magnetic field of 10 kOe. The photoluminescence (PL) measurement was performed at room temperature on a Hitachi F-7000 FL spectrophotometer by a 325-nm excitation from Xe lamp. Zeta potential of the as-synthesized $NiFe_2O_4$ powders was measured at various pH values (from 2 to 10) in 0.01-M NaCl solutions using a Malvern Instrument zetasizer.

Adsorption experiments

Adsorption experiments were done in an Erlenmeyer flask, where 200-ml acid red dye (ARB) solution was placed. The initial concentrations of the dye were changed from 20 to 100 mg L^{-1}. The sealed flask with the dye solution was agitated at a constant speed of 250 rpm in a temperature

controlled shaking water bath at temperatures of 298, 303, 313, and 323 K. The initial pH values of the solution were controlled by 0.1-N HNO_3 or 0.1-N NaOH. When the desired temperature was attained, samples were taken at different time intervals. The dye concentration was determined by a Unicam V2-30 UV-Vis spectrophotometer at a wavelength of 516 nm. The amounts of the adsorbed dye at interval time t, q_t (mg g^{-1}), and after equilibrium reached q_e were calculated according to:

$$q_t = (c_o - c_t)V/m \quad (1)$$

$$q_e = (c_o - c_e)V/m \quad (2)$$

where C_o is the initial ARB concentration, C_t the ARB concentration at any time t, C_e is the equilibrium concentration of ARB in solution, V (L) the volume of the solution, and m (g) is the mass of the adsorbent.

The kinetic features of the dye adsorption onto ferrite samples were studied at pH = 6.5 using 50 mg of the $NiFe_2O_4$ and 50 ml of 50-ppm dye solution at the desired temperature.

Results and discussion

XRD

XRD patterns of the as-prepared $NiFe_2O_4$ ferrite samples (NiF_{micr}, NiF_{ppt}, and NiF_{poly}) are presented in Fig. 1. All the diffraction peaks observed matched well with an inverse spinel crystal structure of $NiFe_2O_4$ (JCPDS file no. 86-2267, Fd-3m), which is realized from the peaks observed at (111), (220), (311), (222), (400), (511), and (440) for all samples. The mean crystallite size (D_{XRD}) of the prepared $NiFe_2O_4$ samples was estimated from the (311) peak by applying Debye-Scherrer's formula (Cullity 1978).

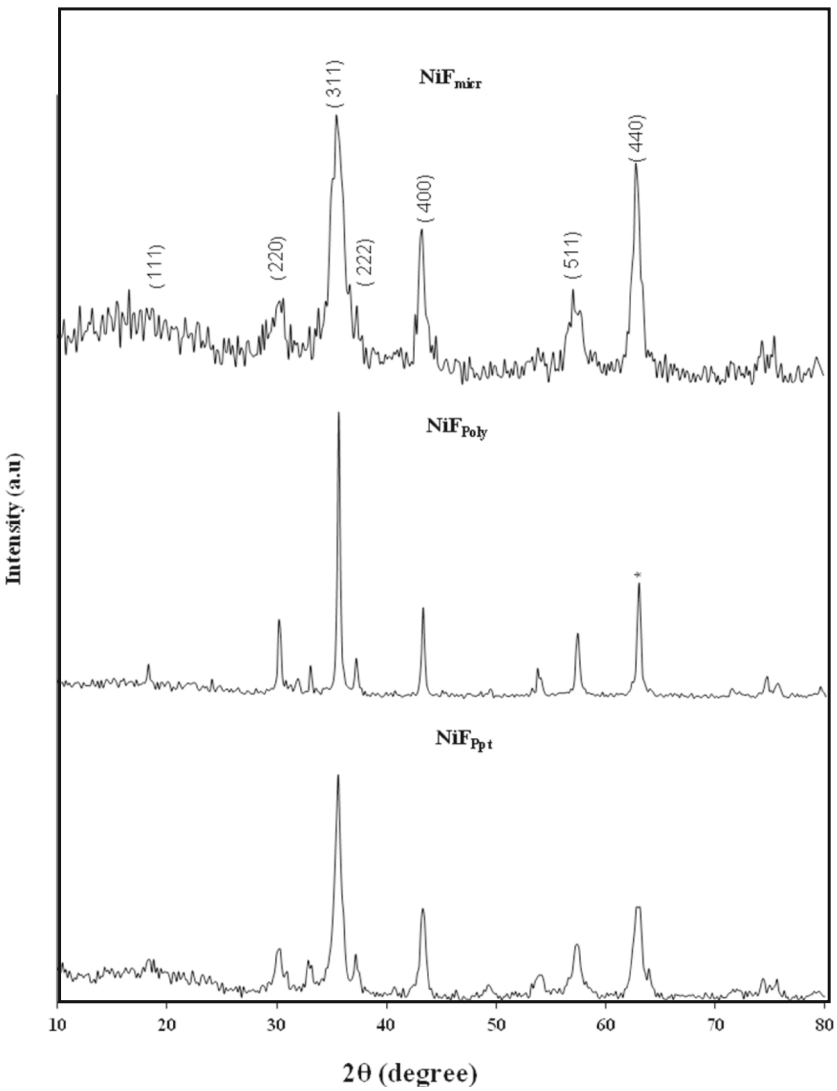

Fig. 1 XRD of the investigated samples

$$D_{XRD} = f\lambda/\beta\cos\theta \quad (3)$$

where f is the shape factor (0.9), θ the angle of the diffraction, β the full-width at half-maximum, and λ the wavelength of X-ray. The average crystallite sizes of the as-prepared $NiFe_2O_4$ ferrite are found to lie in a nanosize range of 11.4–75.4 nm Table 1.

The lattice parameter of the ferrite samples was calculated from the (311) peak using $a = \lambda / 2\sin\theta\ (h^2 + k^2 + l^2)$, where h, k, and l are the Miller indices and found to be $a = 8.362$, 8.369, and 8.372 Å for NiF_{micr}, NiF_{ppt}, and NiF_{poly}, respectively. The X-ray density of the ferrite was also calculated using; $D_{XRD} = 8M / N_A a^3$, where M is the molecular weight, N_A is the Avogadro's number, and a is the lattice parameter and found to be 5.30, 5.26, and 5.25 g/cm^3 for NiF_{micr}, NiF_{ppt}, and NiF_{poly}, respectively.

FT-IR

FT-IR transmittance spectra of $NiFe_2O_4$ specimens show two main absorption bands at $\nu_1 \sim 415$ and $\nu_2 \sim 595$ cm^{-1} for all samples (Fig. S1). Nickel ferrite has the inverse spinel crystal structure; thus, the appeared two absorption bands ($\nu_1$and ν_2) for all samples are assigned to the stretching vibration frequency of the metal-oxygen at the octahedral site Fe^{3+}-O^2 and tetrahedral site Fe^{3+}-O^{2-}, respectively (Gotic et al. 1998). Besides, these vibrational modes, a vibration band at ~ 1625 cm^{-1} due to bending mode of water in addition to a broad hump with a maximum at about 3418 cm^{-1}, were observed (Dutoit et al. 1995).The differences in the area of ν_1 and ν_2 absorptions bands may be attributed to the variation in the preparation methods of the samples or the change in the morphological structure obtained (Deraz 2008).

SEM and TEM

The SEM images of the as-synthesized $NiFe_2O_4$ samples Fig. 2I show that the powders are shaped in agglomerated and separated nanosized $NiFe_2O_4$ particles with surface morphology depending on the preparation method. The SEM-image of NiF_{poly} (Fig. 2I-a) shows surface morphology of nanorods, whereas the SEM image of NiF_{ppt} (Fig. 2I-b) sample shows a limited extent of aggregation and approximately spherical shape particles. On the other hand, NiF_{micr} sample shows the presence of the particles in a flower like structure (Fig. 2I-c). The ferrite samples were further investigated with TEM (Fig. 2II). The particle sizes and the morphologies of the examined samples are listed in Table 1. The spinel $NiFe_2O_4$ exhibits a cubic structure; consequently, the growing direction of the $NiFe_2O_4$ nanorods can be controlled as the [111] crystallographic route, which is the easiest-magnetization axis. This growth direction is predictable to upset the magnetic properties as will be seen in the magnetic section.

UV-Vis study

The effect of the preparation process, crystallite size, and morphological structure on the optical properties of $NiFi_2O_4$ samples was studied using UV-Vis diffuse reflectance spectroscopy. The spectra for all samples demonstrated in Fig. 3 show an absorbance band in the visible region longer than 500 nm and moves to a higher wavelength with increasing the particle size (Table 1). This band is attributed to $^3A_{2g}$ to $^3T_{1g}$ (F) transition of Ni^{2+} octahedrally coordinated by O^{2-} ions (Cui et al. 2009; Dixit et al. 2012). Tauck's equation $[(\alpha h\nu)^n = k'(h\nu - Eg)]$ was used to estimate band gap energy. α is the absorption coefficient, $h\nu$ is the photon energy, k' is the constant relative to the material, and n is either 2 for direct transition or 1/2 for a direct transition (Kreisel et al. 1998). The best fitting is found for indirect transition and showed values of 1.49, 1.52, and 1.56 eV for NiF_{micr}, NiF_{poly}, and NiF_{ppt}, respectively.

Raman study

Figure 4 shows the Raman spectra of $NiFe_2O_4$ samples. The appearing five Raman active modes of $(A_{1g} + E_g + 3F_{2g})$ peaks with shoulders on the low energy side are characteristic peaks of nickel ferrite (Dixit et al. 2012; Graves et al. 1988). These modes have appeared at different wave numbers depending on the crystallite size and the morphological structure as shown in Table 2.The A_{1g} mode occurs as a result of symmetric stretching of oxygen atoms about Fe-O (and Ni-O) bonds in the tetrahedral coordination. E_g mode is attributed to symmetric bending of oxygen atom with reference to cations, and $F_{2g}(3)$ is due to asymmetric bending of oxygen. The shoulder peaks are attributed to the inversion structure of the nickel ferrite lattice. Nickel ferrite has inverse spinel structure and space group of Fd3m.The presence of both Fe^{3+} and Ni^{2+} occupying the octahedral sites causes the separation vibrational frequencies of the NiO_6 and FeO_6 octahedral.

Table 1 Particle size, optical absorption maximum, and surface data of the investigated $NiFe_2O_4$ samples

Samples	Particle size D_{XRD} (nm)	Particle size D_{TEM} (nm)	λ (nm)	V_p (cm^3/g)	S_{BET} (m^2/g)
NiF_{ppt}	11.4	10.5	510,750	0.19	115.3
NiF_{micr}	75.4	72.1	520,760	0.17	36.2
Ni_{Poly}	21.7	Diameter = 6 length = 22	530,770	0.09	82.9

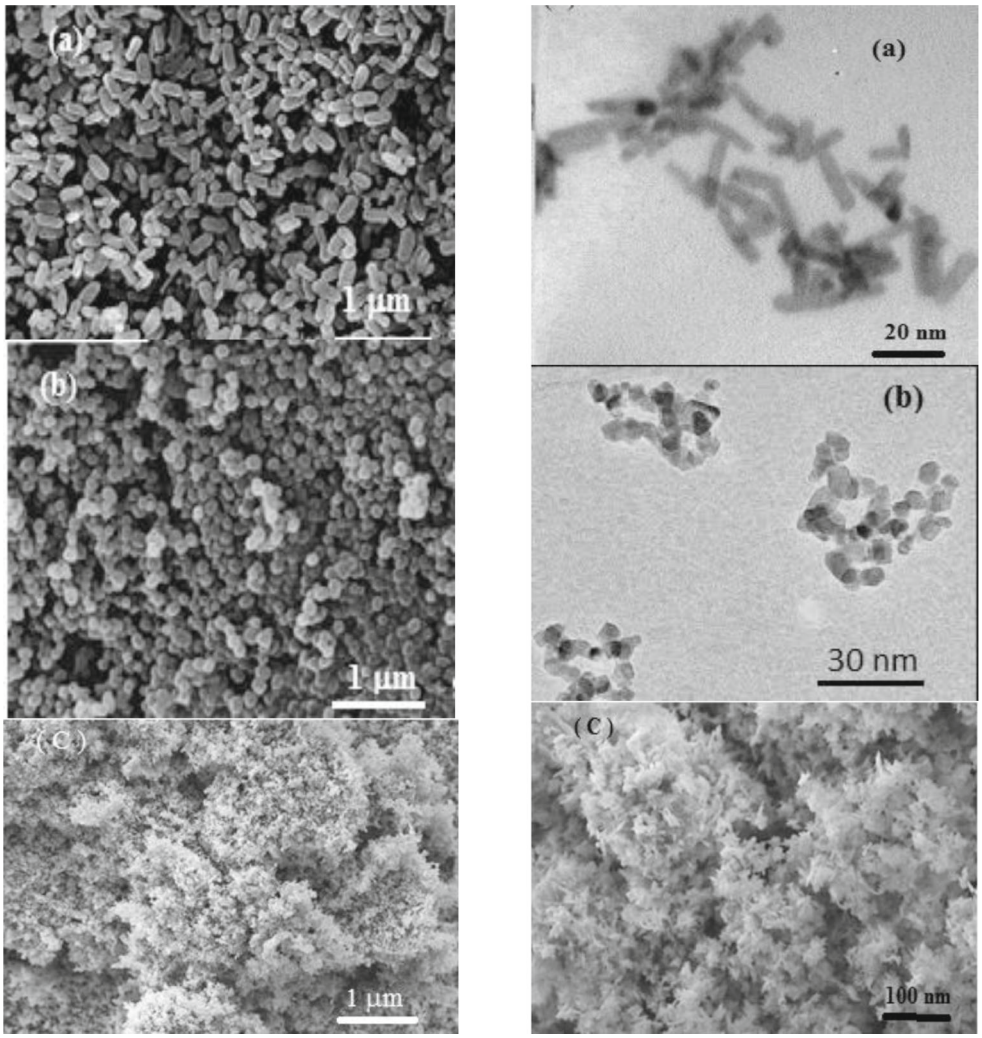

(2-I) (2-II)

Fig. 2 **I** SEM images of **a** NiF_{poly}, **b** NiF_{ppt}, and **c** NiF_{micr} samples. **II** TEM images of **a** NiF_{poly}, **b** NiF_{ppt}, and **c** NiF_{micr} samples

Magnetization results

Magnetization measurements of the nanonickel ferrite samples were performed at room temperature using the VSM technique in the range of − 10 to 10 kOe, and the results obtained are shown in Fig. 5 and summarized in Table 3. The results obtained show superparamagnetic behavior, which is an important property for magnetic targeting carriers (Li et al. 2008). Our M_s and coercivity (H_c) values lie in the range of 24.4–34.8 emu/g and 0.05–1.6.0 Oe, respectively, which

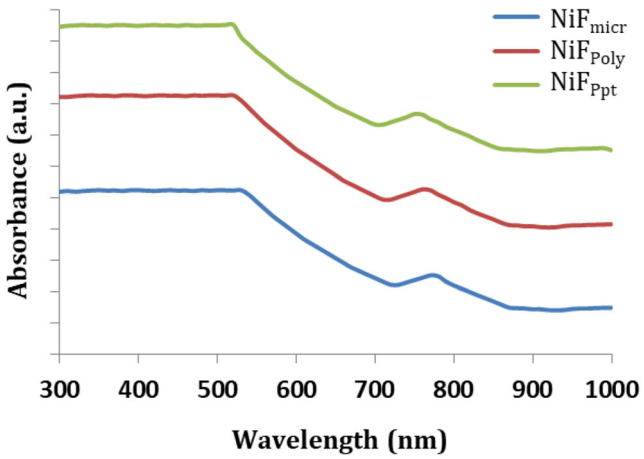

Fig. 3 UV-Vis spectra of $NiFe_2O_4$ samples

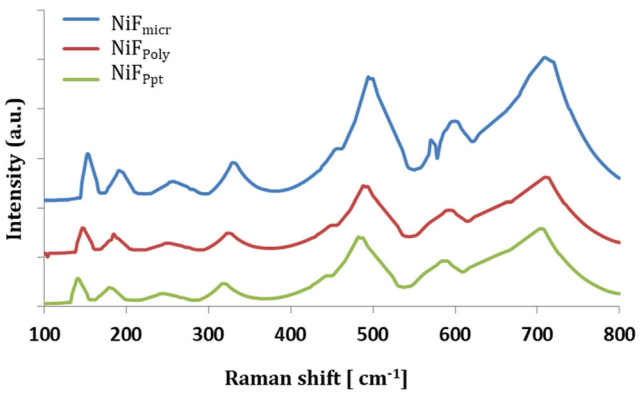

Fig. 4 Raman spectra of the investigated $NiFe_2O_4$ samples

Table 2 Raman mode labels of the investigated samples

Mode label	NiF_{ppt}		NiF_{micr}		NiF_{poly}	
	Wave no. cm^{-1}	Shoulder cm^{-1}	Wave no. cm^{-1}	Shoulder cm^{-1}	Wave no. cm^{-1}	Shoulder cm^{-1}
$F_{2g}(1)$	179	141	182	147	184	153
E_g	318	245	324	251	331	257
$F_{2g}(2)$	482	426	488	433	496	440
$F_{2g}(3)$	587	554	595	540	599	575
A_g	704	652	709	646	711	599

are less than that found by Morrish and Haneda (1981) (M_s = 37.6 emu/g, H_c = 500 Oe for particles with sizes from 60 to 100 nm) due to higher number of surface atoms present in our samples. The nanonickel ferrite can be counted to be collected from two parts, the part of crystal atoms that organize long-range order and an interfacial part (surface atoms) that is reflected the unsystematic and short-range order. The surface atoms raise with increasing the surface area, leading the unsystematic to be major. The unsystematic denotes the occurrence of vacancies, the range of interatomic arrangement, and small coordination number. These grounds can cause a discontinuity in the exchange bonds at the surface, consequently, conducts to hindrance and spin disorder. This disorder may then cause the formation of an inactive surface layer that has small magnetization. With increasing the surface area, this inactive layer will grow leading to reduce the saturation magnetization, as shown in our results. Inspection of Table 1 shows small values ranging from 0.04 to 0.08 for squareness (M_r/M_s). These small values can be attributed to the non-interacting single domain particles with uniaxial magnetocrystalline anisotropy magnetic material with inverse spinel structure in which half of Fe^{3+} fill the tetrahedral A. Moreover, Table 3 shows that there is no general correlation that could be found between the particle size and the magnetic properties of the samples prepared by different techniques. The absence of this correlation reveals that the magnetic properties obtained are affected not only by the size but also by the morphology.

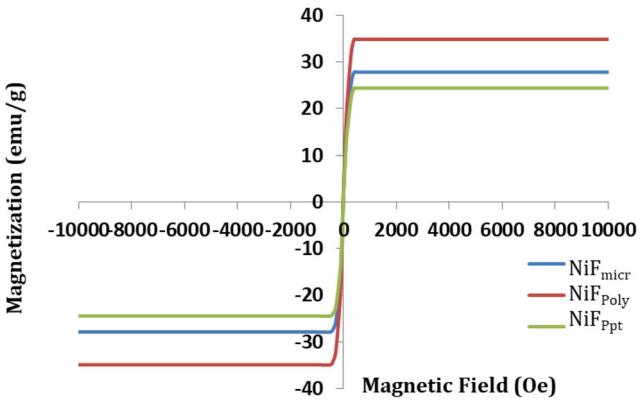

Fig. 5 Magnetic hysteresis of the investigated samples

Surface study

The adsorption phenomena are strongly depending on the physical properties of the solid and particularly on porous texture. The isothermal N_2 adsorption-desorption of the as-prepared nickel ferrite specimens shown in Fig. S2 shows small hysteresis loops (type IV), revealing to the presence of mesopores at high pressure (Putz et al. 2016). The surface data are summarized in Table 1, which shows that the increase in surface area has the order: $NiF_{ppt} > NiF_{poly} > NiF_{micr}$, which goes parallel with decreasing the particle size. Also, the total pore volume increases in the order: $NiF_{ppt} > NiF_{micr} > NiF_{poly}$.

The zeta potentials of $NiFe_2O_4$ samples were measured in water solution at pH in the range 3–11 and decreased from positive to negative values with increasing pH over the whole studied range Fig. S3. The pH pzc of NiF_{micr}, NiF_{poly}, and NiF_{ppt} was found to be 6.5, 6.6, and 6.7, respectively.

Adsorption studies

Adsorption of dye, like for other sorption processes, can be affected by important factors, such as contact time, initial dye concentration, adsorbent dose, pH, and temperature.

Effect of contact time

The impact of contact time on the removal of acid red dye, ARB, by nickel ferrite samples was tested at pH = 6.6, temperature (298 K), 50-mg/L concentration of dye, and 0.1-g nickel ferrite dosage. The results obtained, given in Fig. 6, show that the adsorption of ARB happens very fast during the first 30 min from starting the experiments and then

Table 3 Magnetic data of the investigated $NiFe_2O_4$ samples

Sample	Particle size (nm)	M_s (emu/g)	M_r (emu/g)	H_c (Oe)	M_r/M_s
NiF_{micr}	75.4	24.4	1.3	0.05	0.053
NiF_{ppt}	11.4	27.8	1.1	0.03	0.039
NiF_{poly}	21.7	34.8	2.8	1.6	0.08

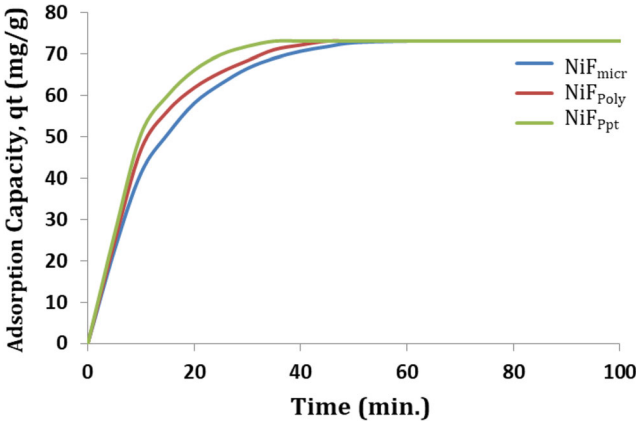

Fig. 6 Effect of contact time on adsorption capacity of the investigated $NiFe_2O_4$ samples

increases slightly to reach an equilibrium state. The equilibrium time has the following order: $NiF_{micr} > NiF_{poly} > NiF_{ppt}$.

Effect of pH

The adsorption of the dye onto ferrite samples was investigated at various pH ranging from 2 to 10 for all three samples. It was found that the dye removal, for all samples, increases with raising the pH and attains a maximum value at pH 6.6, and after that largely decreases, a typical plot is shown in Fig. S4a). The higher values of adsorption observed at acidic and neutral pH may be attributed to the electrostatic attraction between $NiFe_2O_4$ with a positive charge and negatively charged acid dye. However, it was observed that in the alkaline medium, the dye removal drastically decreases, which might be attributed to the adsorption of hydroxyl ions and consequently competition to adsorption active sites with the dye molecules.

Influence of adsorbent dosage

The impact of adsorbent dose (0.1 to 1.0 g/L) on the dye removal, while keeping other parameters (concentration of dye = 50 mg/L and pH = 6.5) constant, was investigated for all the three samples. The results given in Fig. S4b showed a fast increase in the dye removal yield with increasing the dosages of the ferrite sample to attain a constant value at higher dosage of 0.4, 0.5, and 0.6 g/L for NiF_{ppt}, NiF_{poly}, and NiF_{micr}, respectively. The increase in the adsorption yield can be due to the increase in the number of adsorption sites as well as active surface area available for adsorbent-dye interaction (Zhang et al. 2007).

Effect of initial dye concentration

The impact of dye concentration on the removal percentage of the dye was also studied for all the three ferrite samples by changing the concentration from 20 to 100 mg/L, all other parameters kept constant. At a dye concentration of 20 mg/L, the dye was completely removed at ~ 30 min. As the concentration increases, the dye was not completely removed, typical plot shown in Fig. S4c). This means that at low concentrations, the binding sites on the surface of adsorbent were available to all the dye molecules present in the solution. At high concentrations, the adsorption capacity was decreased owing to the adsorption sites saturation.

Adsorption isotherm

The equilibrium adsorption isotherms are one of the most important figures that help to realize the mechanism of adsorption and describe how adsorbates could interact with adsorbents. In the present work, our adsorption data have been analyzed using the Langmuir, the Freundlich, and the Temkin isotherm models (Adamson and GAST 1990; Foo and Hameed 2010; Demiral and Gunduzoglu 2010; Aharoni and Ungarish 1977).

Langmuir isotherm Langmuir isotherm model is an empirical model applicable to homogeneous adsorption and supposing that adsorption only occurs at a limited number of identical sites on the surface to form an adsorbed monolayer. The model presumes equal energies of adsorption onto the surface and the absence of any interaction between the adsorbate molecules. The linear form of this isotherm is signified by the expression (Adamson and GAST 1990).

$$C_e/q_e = (1/bq_m) + C_e/q_m \quad (4)$$

where q_m is correlated to the capacity of monolayer adsorption, and b is the Langmuir adsorption equilibrium constant. Through the plots of C_e/q_e versus C_e (typical plot shown in Fig. S5a), the q_m and b values were calculated and listed in Table 4.

Table 4 The Langmuir, Freundlich, and Temkin parameters of adsorption isotherms of ARB onto investigated $NiFe_2O_4$ samples

Sample	NiF_{ppt}	NiF_{poly}	NiF_{micr}
Langmuir			
$q_{e\ (exp)(mg/g)}$	72.5	73.5	73.7
q_e (calcul)	151.5	155	161
b	1.53	1.55	1.61
R^2	0.9723	0.9712	0.9705
Freundlich			
n	3.41	3.53	3.61
K_f (L/g)	80.4	82.5	84.1
R^2	0.9899	0.9923	0.9911
Temkin isotherm			
K_T (L/mg)	75.65	78.1	79.7
B_1 (kJ/mol)	20.37	19.82	18.99
R^2	0.8871	0.8532	0.8213

Freundlich adsorption isotherm The Freundlich isotherm model describes the non-ideal and reversible adsorption, which is related to multilayer adsorption based on a postulation relating the energetic surface heterogeneity (Foo and Hameed 2010). The linear form equation of the model is given by the equation:

$$\ln q_e = \ln K_f + (1/n) ln C_e \quad (5)$$

where K_f is the estimated adsorption capacity, and $1/n$ denotes the adsorption intensity and also the kindness of adsorption (Demiral and Gunduzoglu 2010). For $n = 1$, the division between the two phases are unconnected with the concentration, and for normal adsorption, the value of $1/n$ lies below one. On the other hand, the values of $1/n$ above one refer to cooperative adsorption. To calculate the constants of the Freundlich equation, we plot $\ln q_e$ diagram vs. $\ln C_e$, and the slope of this plot is n and the intercept is $\ln K_f$. Typical plot shown in Fig. S5b), and parameters K_f and n are listed in Table 4.

Temkin isotherm This isotherm contains a factor that clearly considers the sorbent-sorbate interactions. It supposes that the lessening in the heat of adsorption is linear instead of logarithmic, as inferred in the Freundlich isotherm (Aharoni and Ungarish 1977). The linear form of the Temkin equation is given by:

$$q_e = B_1 ln K_T + B_1 ln C_e \quad (6)$$

where K_T is the equilibrium binding constant associated to the maximum binding energy, and $B_1 = RT / b$ is connected to the adsorption heat. The isotherm constants are determined from plotting q_e against $\ln C_e$. Typical plot is shown in Fig. S5c, and parameters K_T and B_1 are listed in Table 4.

Adsorption kinetics and thermodynamics

Several kinetic models have been applied to define the solute uptake rate, which in turn dominates the residence time of sorption reaction and the governing mechanism of dye adsorption from aqueous solution. In our study, the linear forms of the pseudo-first-order Lagergren (Eq. (7)) (Lin et al. 2009), pseudo-second-order rate equation (Eq. (8)) (Ho and McKay 1999), second order (Eq. (9)) (Ho 2006), Elovisch (Eq. (10)) (Wu et al. 2009), and intra-particle diffusion (Eq. (11)) (Schierz and Zanker 2009) were applied, and the obtained results are represented in Figs. 7, 8 and summarized in Table 5. The obtained correlation coefficients for various kinetic models were used to evaluate the consistency between the experimental and predicted data.

$$log\ (q_e - q_t)/qe = qe - (kL/2.303)t \quad (7)$$

$$(t/q_t) = \left(1/k_1 q_e^{\,2}\right) + t/q_e \quad (8)$$

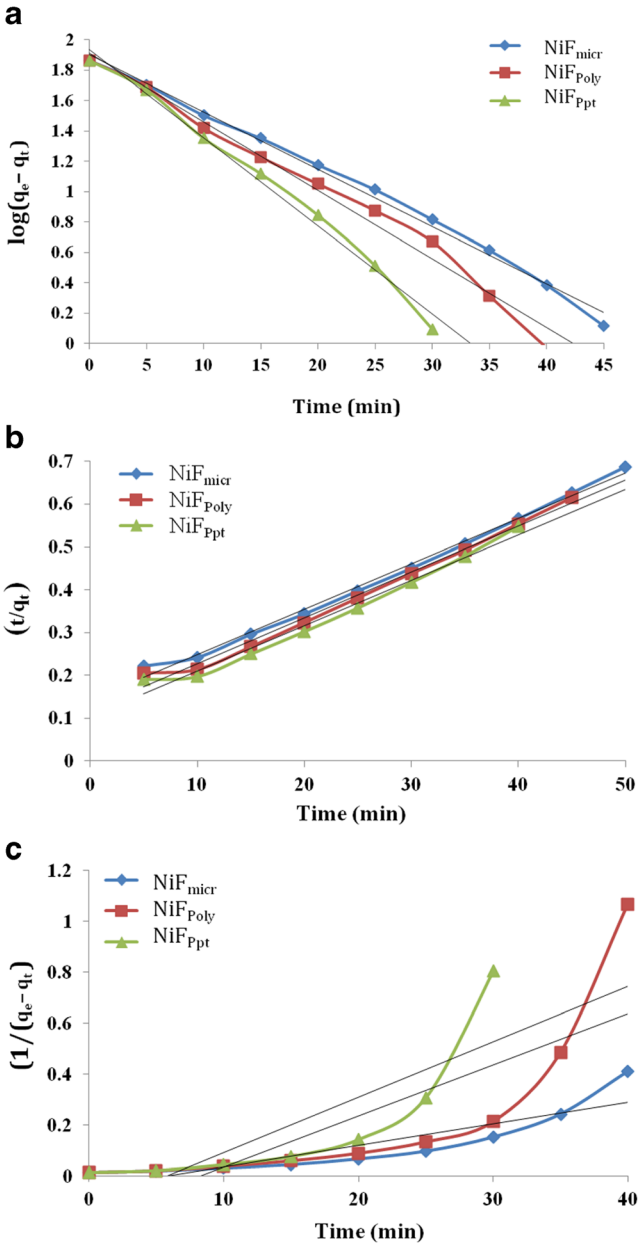

Fig. 7 **a** Pseudo-first-order plot for the adsorption of ARB onto $NiFe_2O_4$ samples (ads. dosage = 0.5 g/L, pH = 6.6, T = 298 K, agitation = 250 rpm). **b** Pseudo-second-order plot for the adsorption of ARB onto $NiFe_2O_4$ samples (ads. dosage = 0.5 g/L, pH = 6.6, T = 298 K, agitation = 250 rpm). **c** Second-order plot for the adsorption of ARB onto $NiFe_2O_4$ samples (ads. dosage = 0.5 g/L, pH = 6.6, T = 298 K, agitation = 250 rpm)

$$(1/(q_e - q_t) = (1/q_e) + k_2 t) \quad (9)$$

$$q_t = \left(1/\beta'\right) ln\left(\alpha'/\beta'\right) + \left(1/\beta'\right) ln(t) \quad (10)$$

$$q_t = K_{dif} t^{0.5} + C \quad (11)$$

where k_L, k_1, and k_2 are the rate constants for Lagergren pseudo-first-order model, second-order model, pseudo-second-order model, respectively; α' and β' are the initial

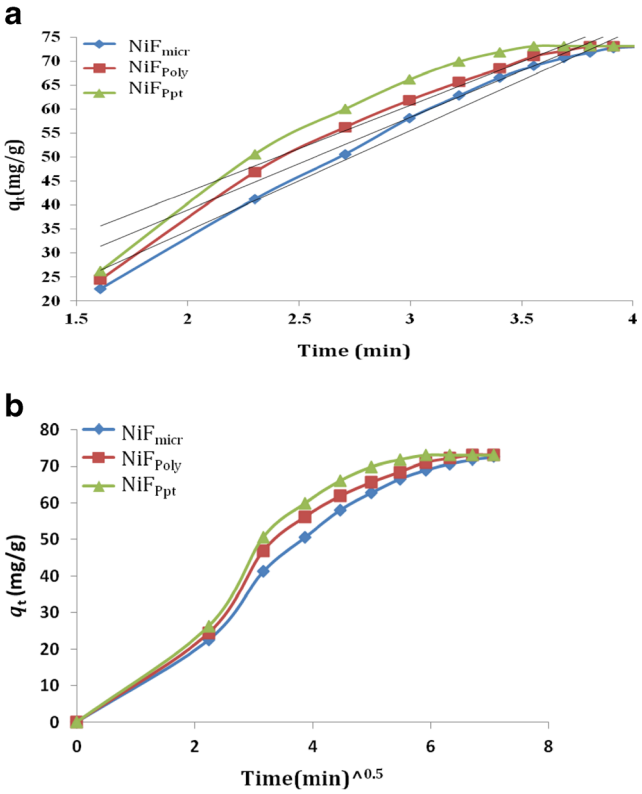

Fig. 8 **a** Elovisch plot for the adsorption of ARB onto $NiFe_2O_4$ samples (ads. dosage = 0.5 g/L, pH = 6.6, T = 298 K, agitation = 250 rpm). **b** Intra-particle diffusion plot for the adsorption of ARB onto $NiFe_2O_4$ samples (ads. dosage = 0.5 g/L, pH = 6.6, T = 298 K, agitation = 250 rpm)

adsorption rate and desorption constant, respectively; K_{diff} is the intra-particle diffusion rate constant.

For all three samples, the pseudo-second-order kinetic model gave the best fit for experimental data as $R^2 \geq 0.99$, and the calculated q_e values are close to that of the experimental values Table 5. Hence, the pseudo-second-order model is predominant for explaining the ARB adsorption mechanism onto the different morphological structures of nickel ferrite samples.

Reusability of $NiFe_2O_4$

The nano-$NiFe_2O_4$ (NiF_{micr}) sample was recovered using magnetic separation by means of a permanent magnet. The sample was cleaned by washing three times by NaOH solution of pH 0.1; after that, the adsorption was performed to assess the reusability of ferrite sample. The results showed that the removal of ARB by ferrite samples only reduced after the first cycle and then reaches almost steady state in the following cycles to be 96, 95, and 93% after ten cycles for NiF_{micr}, NiF_{poly}, and NiF_{ppt}, respectively. It means that $NiFe_2O_4$ can be used repeatedly over many cycles for removing ARB from the water.

Table 5 Adsorption kinetic parameters at initial ARB 50 ppm onto 0.5 g/L of $NiFe_2O_4$ at pH 6.6, T = 298 K; agitation = 250 rpm

Sample	NiF_{ppt}	NiF_{poly}	NiF_{micr}
Pseudo-first-order			
k_1 (L/min)	0.0251	0.0181	0.0183
q_e (calc) (mg/g)	1.18	1.261	1.0325
R^2	0.9898	0.969	0.9914
Second-order			
k_2 (g (mg min)$^{-1}$	0.0217	0.0201	0 .0085
q_e (calc) (mg/g)	8.02	5	20
R^2	0.6799	0.6372	0.7814
Pseudo-second-order			
K' (gmg^{-1} min^{-1})	7.92E-04	9.48E-04	9.18E-04
q_e (calc), (mg/g)	94.3	94.3	94.4
R^2	0.9941	0.9899	0.9899
Intra-particle diffusion			
K_{dif} (mg g^{-1} min$^{-.5}$)	10.757	10.659	10.588
C	4.15	7.03	9.57
R^2	0.9577	0.9279	0.8885
Elovich			
β (g/mg^{-1})	0.055	0.0516	0.0477
A (mg(g min)$^{-1}$	26.01	19.57	14.86
R^2	0.8745	0.9352	0.971
$q_{e\ (exp)}$	72.5	73.5	73.7

Effect of temperature on thermodynamic parameters

Thermodynamic considerations of an adsorption process are necessary to conclude whether the process is spontaneous or not. Thermodynamic experiments were operated at 298, 303, 313, and 323 with a 50-mg/L dye concentration and a 0.5-g/L mg adsorbent dosage. These thermodynamic parameters were calculated using Eqs. (12–14):

Table 6 Thermodynamic parameters for the adsorption of ARB dye onto investigate $NiFe_2O_4$ samples

Sample	Temperature (K)	$\Delta H°$ (kJ/mol)	$\Delta S°$ (J/mol K)	$\Delta G°$ (kJ/mol)
NiF_{ppt}	298	16.92	89.2	− 9.63
	303			− 10.10
	313			− 10.99
	323			− 11.89
NiF_{poly}	298	15.11	82.3	− 9.44
	303			− 9.82
	313			− 10.64
	323			− 11.47
NiF_{micr}	298	14.73	79.02	− 8.82
	303			− 9.21
	313			− 9.99
	323			− 10.79

$$\Delta G^\circ = \Delta H^\circ - T\Delta S^\circ \quad (12)$$

$$\Delta G^\circ = -RT\ln K_c \quad (13)$$

$$K_c = C_s/C_e \quad (14)$$

where K_c, the equilibrium constant, is the ratio of the equilibrium concentration of the dye (q_e) attached to adsorbent to the remaining concentration of the dye in the solution at equilibrium. The values of ΔH° and ΔS° are decided from the slope and intercept of a linear plot between $\ln K_c$ and $1/T$, respectively, and listed in Table 6.

The ΔG° values were negative at each one of the experimental temperature referring to the achievability of the process and the spontaneous class of the adsorption (Fernandes et al. 2010). For ΔG° values ranging between (−20 to 0) kJ mol^{-1}, the physisorption is the main mechanism of the adsorption process.

The obtained positive value of ΔS° refers to the increase in the randomness during the dye adsorption process and suggesting the affinity of ARB molecules on the surface of ferrite adsorbents. The positive value of ΔH° indicates that the adsorption process is endothermic; thus, higher temperatures will accelerate the adsorption of dye onto the adsorbate. The range of enthalpy ΔH° gives an idea about the adsorption type (physically, lower than 40 kJ mol^{-1} or chemically, 40–120 kJ mol^{-1}) (Sapawe et al. 2013). In our study, ΔH° values lie in the range of physisorption, referring to the physical characteristics of the adsorption. This means that the interaction between ARB molecules and active sites on the ferrite samples surface was mainly electrostatic.

Conclusions

$NiFe_2O_4$ nanoparticles have prepared through three different methods, namely, microwave (NiF_{micr}), co-precipitation (NiF_{ppt}), and polymeric pyrolysis (NiF_{poly}). XRD analyses showed the formation of inverse spinel structure, single phase, for all samples. NiF_{poly} sample showed a nanorod morphological structure with a length of 6 nm and diameter of 22 nm; NiF_{micr} showed nanoflower structure, whereas NiF_{ppt} showed a deformed spherical nanoparticles with a diameter of 11.4 nm. Magnetic hysteresis loops approved the superparamagnetic behavior for all samples. The magnetic saturation (Ms) of the NiF_{poly} sample with rod structure exhibits the highest saturation value 34.8 emu/g. The prepared $NiFe_2O_4$ samples were subjected for the removal of ARB as an anionic azo dye model from synthetic wastewater. The adsorption parameters studied are dye concentration, pH, contact time, adsorbent dosage, temperature, and morphological structure of ferrite. The best pH value for favorable dye adsorption was 6.5–6.7. The results showed that the prepared ferrite effectively removes acidic red dye in short contact time with higher removal percentage of 99% at optimum condition. The sorption data fitted into Langmuir, Freundlich, and Temkin isotherms out of which Freundlich Adsorption model was found to behave the best fitting data. The kinetic results showed that the pseudo-second-order is the best model to describe the adsorption mechanism of the ARB onto NFNs. Thermodynamics studies showed that adsorption of ARB on ferrite samples is endothermic and took place spontaneously in nature. The prepared magnetic nanosorbent showed considerable high stability, high adsorption capability, and magnetically separation capability. The morphological structure did not affect the adsorption mechanism, but the nanorod structure showed better absorptivity for ARB from aqueous solution.

References

Allen SJ (1996) Types of adsorbent materials-use of adsorbents for the removal of pollutants from wastewaters, vol 59. CRC, Boca Raton, FL, USA

Aharoni C, Ungarish M (1977) Kinetics of activated chemisorption. Part 2.—theoretical models. J Chem Soc Faraday Trans 73(1):456–464

Adamson AW, GAST AP (1990) Physical chemistry of surfaces, 5th edn. John Wiley & Sons, New York

Carta D, Casula MF, Falqui A, Loche D, Mountjoy G, Sangregorio C, Corrias A (2009) A structural and magnetic investigation of the inversion degree in ferrite nanocrystals MFe_2O_4 (M = Mn, Co, Ni). J Phys Chem C 113(20):8606–8615

Cullity BD (1978) Elements of X-ray diffraction. Addison-Wesley, USA

Cui B, Lin H, Liu YZ, Li JB, Sun P, Zhao XC, Liu CJ (2009) Photophysical and photocatalytic of core-ring structured $NiFe_2O_4$ nanoplatelets. J Phys Chem C 113:14083–14087

Dawood S, Sen TK (2014) Review on dye removal from its aqueous solution into alternative cost effective and non-conventional adsorbents. J Chem Proc Eng 1:1–11

Dutoit DCM, Schmeider M, Baiker A (1995) Titania-silica mixed oxides: influence of sol-gel and drying conditions on structural properties. J Catal 153(1):165–176

Deraz NM (2008) Production and characterization of pure and doped copper ferrite nanoparticles. J Anal Appl Pyrolysis 82(2):212–222

Dixit G, Singh JP, Srivastava RC, Agrawal HM, Choudhary RJ (2012) Structural, magnetic and optical studies of nickel ferrite thin films. J Adv Mat Lett 3(1):21–28

Demiral H, Gunduzoglu G (2010) Removal of nitrate from aqueous solutions by activated carbon prepared from sugar beet bagasse. J Bioresour Technol 101(6):1675–1680

Farghali A, Bahgat M, Elrouby W, Khedr M (2013) Decoration of multiwalled carbon nanotubes (MWCNTs) with different ferrite nanoparticles and its use as an adsorbent. J Nano stru Chem 3:1–13

Foo KY, Hameed BH (2010) Insights into the modeling of adsorption isotherm systems. J Chem Eng 156:2–10

Fernandes AN, Almeida CAP, Debacher NA, Sierra MMS (2010) Isotherm and thermodynamic data of adsorption of methylene blue from aqueous solution onto peat. J Mol Struct 982(1–3):62–65

Gómez V, Larrechi MS, Callao MP (2007) Kinetic and adsorption study of acid dye removal using activated carbon. Chemosphere 69(7):1151–1158

Goldman A (2006) Modern ferrite technology. J Spri Sci Business Media

Gunjakar JL, More AM, Gurav KV, Lokhande CD (2008) Chemical synthesis of spinel nickel ferrite ($NiFe_2O_4$) nano-sheets. J Appl Surf Sci 254:5844–5848

Gotic M, Czako-Nagy I, Popovic S, Music S (1998) Formation of nanocrystalline $NiFe_2O_4$. J Philos Magn Lett 78:193–201

Graves PR, Johnston C, Campaniello J (1988) Raman scattering in spinel structure ferrites. J Mat Res Bull 23(11):1651–1660

Ho YS, McKay G (1999) Pseudo-second order model for sorption processes. J Process Biochem 34(5):451–465

Ho YS (2006) Review of second-order models for adsorption systems. J Haz MatB 136(3):681–689

Ismail B, Hussain ST, Akram S (2013) Adsorption of methylene blue onto spinel magnesium aluminate nanoparticles: adsorption isotherms, kinetic and thermodynamic studies. J Chem Eng 219:395–402

Kreisel J, Lucazeau G, Vincent H (1998) Raman spectra and vibrational analysis of $BaFe_{12}O_{19}$ hexagonal ferrite. J Solid State Chem 137(1): 127–137

Liu XM, Guo Y, Fu SY (2007) Mass synthesis of nanocrystalline spinel ferrites by a polymer-pyrolysis route. J Mat Sci Eng C 27:750–755

Lowell S, Shields JE, Thomas MA, Thommes M (2004) Characterization of porous solids and powders: surface area, pore size and density. Kluwer Academic Publishers, Dordrecht, Boston, London

Li G-y, Jiang Y-R, K-l H, Ding P, Chen J (2008) Preparation and properties of magnetic Fe_3O_4-chitosan nanoparticles. J Alloys Compd 466(1–2):451–456

Lin JPQY, Zhang XH, Yan Y (2009) Kinetic parameters and mechanisms of the batch biosorption of Cr(VI) and Cr(III) onto Leersia hexandra Swartz biomass. J Colloid Interface Sci 333(1):71–77

Mahmoodi NM, Abdi J, Bastani D (2014) Direct dyes removal using modified magnetic ferrite nanoparticle. J Environ Health Sci Eng 12(96):1–10

Morrish AH, Haneda K (1981) Magnetic structure of small $NiFe_2O_4$ particles. J Appl Phys 52:2496

Putz AM, Len A, Ianăşi C, Savii C, Almásy L (2016) Ultrasonic preparation of mesoporous silica using pyridinium ionic liquid. Korean J Chem Eng 33(3):749–754

Reddy CVG, Manorama SV, Rao VJ (1999) Semiconducting gas sensor for chlorine based on inverse spinel nickel ferrite. J Sens Actuators B 55(1):0–95

Sonali LD, Suryavanshi SS, Mulla IS (2009) Nanostructured nickel ferrite: a liquid petroleum gas sensor. J Ceram Int 35(5):1793–1797

Schierz A, Zanker H (2009) Aqueous suspensions of carbon nanotubes: surface oxidation, colloidal stability and uranium sorption. Environ Pollut 157(4):1088–1094

Sapawe N, Jalil AA, Triwahyono S, Shah M, Jusoh R, Salleh NFM, Hameed BH, Karim AH (2013) Cost-effective microwave rapid synthesis of zeolite NaA for removal of methylene blue. J Chem Eng 229:388–398

Wang L, Li J, Wang Y, Zhao L, Jiang Q (2012) Adsorption capability for Congo red on nanocrystalline MFe_2O_4 (M = Mn , Fe, Co, Ni) spinel ferrites. J Chem Eng 72:181–182

Wu FC, Tseng RL, Juangc RS (2009) Characteristics of Elovich equation used for the analysis of adsorption kinetics in dye-chitosan systems. J Chem Eng 150(1–2):366–373

Zhang G, Qu J, Liu H, Adrienne TC, Wu R (2007) $CuFe_2O_4$/activated carbon composite: a novel magnetic adsorbent for the removal of acid orange II and catalytic regeneration. Aust J Chem 68(6):1058–1066